

CENTRAL RESEARCH LIBRARY.

ORNL-TM-4407

Cy 2

OAK RIDGE NATIONAL LABORATORY LIBRARIES



3 4456 0550275 6

THE EFFECTS OF BONE IN THE
USE OF NEGATIVELY CHARGED PIONS IN
CANCER RADIOTHERAPY

R. T. Santoro
R. G. Alsmiller, Jr.
K. C. Chandler

OAK RIDGE NATIONAL LABORATORY
CENTRAL RESEARCH LIBRARY
DOCUMENT COLLECTION

LIBRARY LOAN COPY

DO NOT TRANSFER TO ANOTHER PERSON

If you wish someone else to see this
document, send in name with document
and the library will arrange a loan.

UCN-7969
(3 3-67)



OAK RIDGE NATIONAL LABORATORY

OPERATED BY UNION CARBIDE CORPORATION • FOR THE U.S. ATOMIC ENERGY COMMISSION

This report was prepared as an account of work sponsored by the United States Government. Neither the United States nor the United States Atomic Energy Commission, nor any of their employees, nor any of their contractors, subcontractors, or their employees, makes any warranty, express or implied, or assumes any legal liability or responsibility for the accuracy, completeness or usefulness of any information, apparatus, product or process disclosed, or represents that its use would not infringe privately owned rights.

Contract No. W-7405-eng-26

Neutron Physics Division

THE EFFECTS OF BONE IN THE USE OF NEGATIVELY CHARGED
PIONS IN CANCER RADIOTHERAPY*

R. T. Santoro
R. G. Alsmiller, Jr.
K. C. Chandler[†]

Note:

This work was funded
by the
NATIONAL SCIENCE FOUNDATION
under Order
NSF/RANN AG-399

FEBRUARY 1974

*Submitted for journal publication.

[†]Computer Sciences Division.

NOTICE This document contains information of a preliminary nature
and was prepared primarily for internal use at the Oak Ridge National
Laboratory. It is subject to revision or correction and therefore does
not represent a final report.

OAK RIDGE NATIONAL LABORATORY
Oak Ridge, Tennessee, 37830
operated by
UNION CARBIDE CORPORATION
for the
U. S. ATOMIC ENERGY COMMISSION



3 4456 0550275 6



Abstract

The effects of bone in the use of negatively charged pions in cancer treatment planning have been estimated using Monte Carlo methods. The influence of bone along the pion path and also the influence of a bone-tissue interface parallel to the direction of motion of the pions have been considered. Calculated results of absorbed dose, cell-survival probability, oxygen enhancement ratio, and relative biological effectiveness as a function of spatial coordinates in a 30-g-cm⁻²-thick tissue phantom with bone both included and excluded are presented. All of the biological data reported here are for T-1 human kidney cells. The extent to which the effects of bone in the path of the pion beam can be approximated by using results for tissue and measuring depth in the phantom in g cm⁻² is considered and discussed.

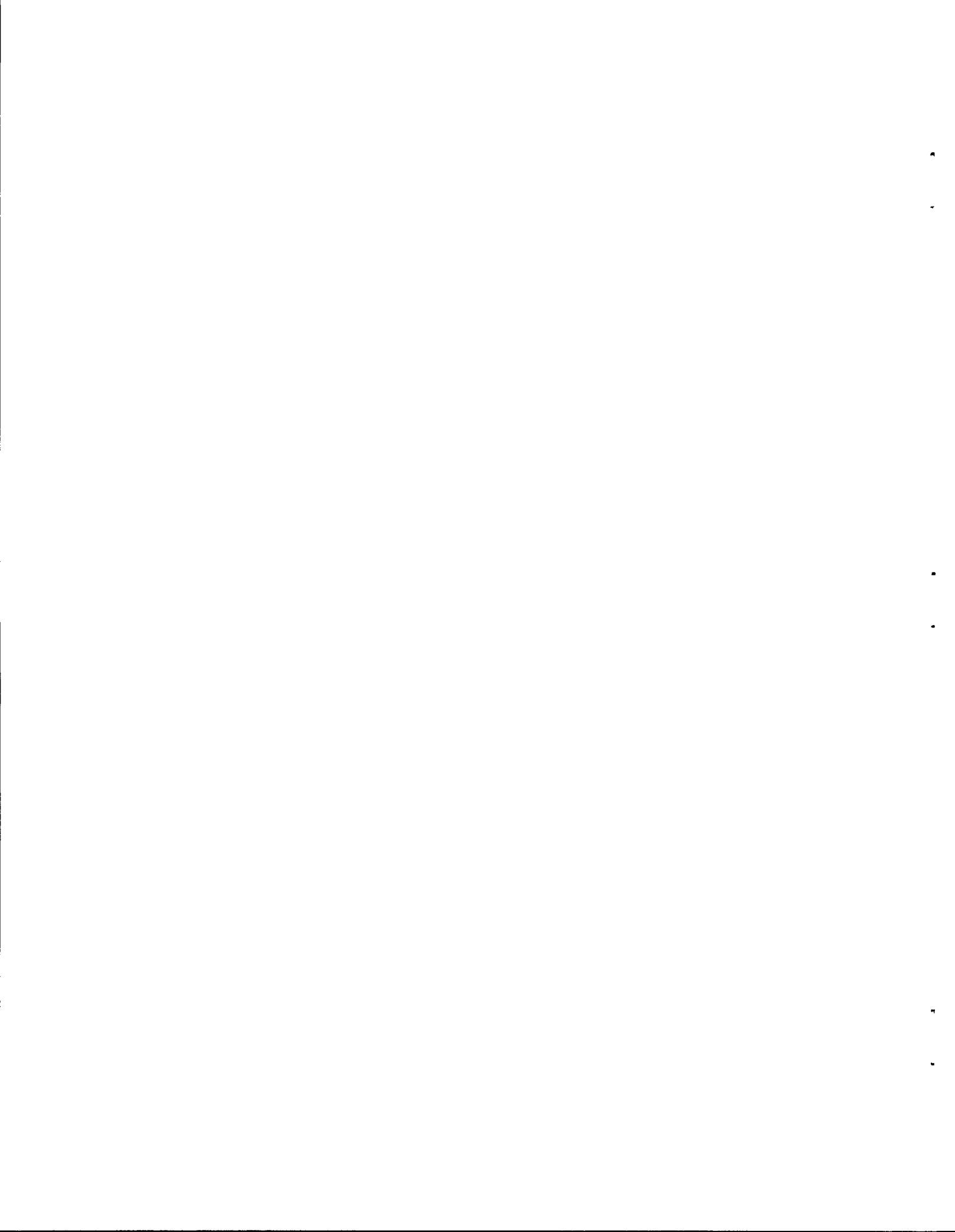
ACKNOWLEDGMENTS

The authors wish to thank R. Hutson of the Los Alamos Scientific Laboratory for suggesting this problem. We are particularly grateful to T. W. Armstrong of the Oak Ridge National Laboratory for numerous helpful discussions throughout the course of this work.

1. INTRODUCTION

It is thought that the use of negatively charged pions in cancer radiotherapy offers marked advantages over those radiations conventionally employed because negatively charged pions have properties which, in principle, allow for better localization of dose and improved biological effectiveness (Fowler and Perkins 1961, Raju and Richman 1970, Rosen 1968). However, when negatively charged pions are used to irradiate a tumor, the pions may or may not pass through bone before coming to rest and being captured in the vicinity of the tumor. Since the chemical composition and density of bone are considerably different from those of tissue, it is necessary to know how the presence of bone along the pion path should be taken into account in treatment planning. To gain some insight into this question, Monte Carlo calculations have been carried out to estimate the spatial distributions of the absorbed dose, the cell-survival probability, the relative biological effectiveness (RBE), and the oxygen enhancement ratio (OER) when negatively charged pions are incident on a tissue phantom with bone both present and absent along the pion path. All of the biological data reported here are for T-1 human kidney cells. The calculated results with bone present and absent are compared and the extent to which the effects of bone may be approximated by using results for tissue and measuring depth in the phantom in g cm^{-2} is considered and discussed.

The methods of the calculations, the tissue-phantom-bone geometries, and the incident-pion-beam characteristics are discussed in the next section, and the results are presented in the last section.



2. DETAILS OF THE CALCULATIONS

The calculated results reported in this paper were obtained using the three-dimensional nucleon-meson transport code HETC (Chandler and Armstrong 1972). This code, along with the cross-section data and reaction models used in the code, has been described in detail elsewhere (Chandler and Armstrong 1972, Alsmiller, Armstrong and Coleman 1970, Armstrong, Alsmiller, Chandler and Bishop 1972, Armstrong 1972, Armstrong, Alsmiller and Chandler 1973, Armstrong and Chandler 1973) and will not be discussed here. HETC has been used to estimate the absorbed-dose distributions and cell-survival probabilities in tissue due to incident nucleons and pions, and in general, good agreement has been obtained between the calculated results and experimental data (Armstrong and Bishop 1971, Armstrong and Chandler 1972, Armstrong and Chandler 1973, Alsmiller and Barish 1974).

The code HETC, as described by Chandler and Armstrong (1972), does not yield directly the absorbed dose, cell-survival probability, RBE, and OER. Monte Carlo methods are used in HETC to simulate particle transport; i.e., the energy, direction, and spatial coordinates of the incident pions are selected from an input source description, and the individual trajectories of the primary pions and the secondary particles produced by nuclear collisions and by pion and muon decay are computed. Each particle in the cascade is followed until it escapes from the phantom, undergoes absorption, or comes to rest. A complete description of each "event" (nuclear interaction, stopped charged particle, etc.) that occurs during the computation of each particle history is stored on magnetic tape. These history tapes are analyzed to obtain results of interest. The methods employed to analyze

these tapes to compute the spatial dependence of the absorbed doses, the cell-survival probabilities, the RBE's, and the OER's are described elsewhere (Armstrong and Chandler 1973). The cell-survival probabilities, the RBE's, and the OER's reported here were calculated for T-1 human kidney cells using the cell-inactivation model of Katz *et al.* (Katz, Ackerson, Homayoonfar and Sharma 1971, Katz, Sharma and Homayoonfar 1972) and the methods described by Armstrong and Chandler (1973).

The tissue-phantom geometries considered in the calculations are shown schematically in fig. 1 as (a), (b), (c), and (d): (a) is a homogeneous tissue phantom 30 g cm^{-2} thick, (b) is a tissue phantom 30 g cm^{-2} thick having a 2-g-cm^{-2} -thick bone slab inserted at a depth of 1 g cm^{-2} , (c) is a tissue phantom 30 g cm^{-2} thick having a 2-g-cm^{-2} -thick bone slab at a depth of 9 g cm^{-2} , and (d) is a tissue phantom 30 g cm^{-2} thick having a 4-g-cm^{-2} -thick bone slab, with a 2.5-cm -radius hole about the axis of symmetry, at a depth of 2 g cm^{-2} . In all cases, the phantoms are assumed to be infinite in direction perpendicular to the axis of symmetry. Here and throughout this paper, the thickness z' , in g cm^{-2} , at radius r is defined by the equation

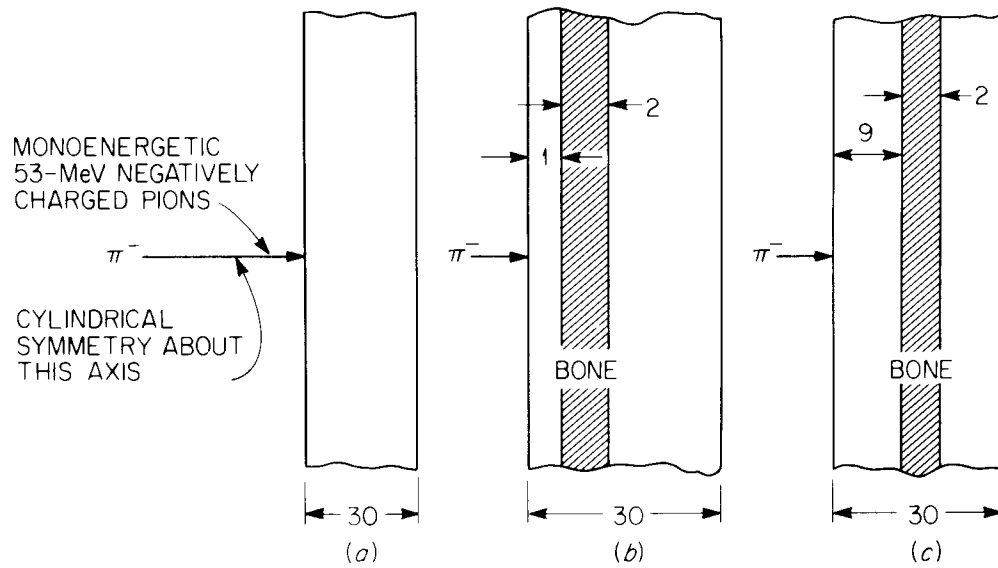
$$z' = \int_0^z \rho(r, z'') dz'' ,$$

where

r, z = cylindrical coordinates in cm,

$\rho(r, z)$ = the density of the phantom at an r, z point in g cm^{-3} .

The composition and density of the bone and tissue used in the calculations are given in table 1.



NOTE : UNSHADED AREAS ARE TISSUE
DIMENSIONS ARE IN $g\ cm^{-2}$ EXCEPT WHERE SHOWN

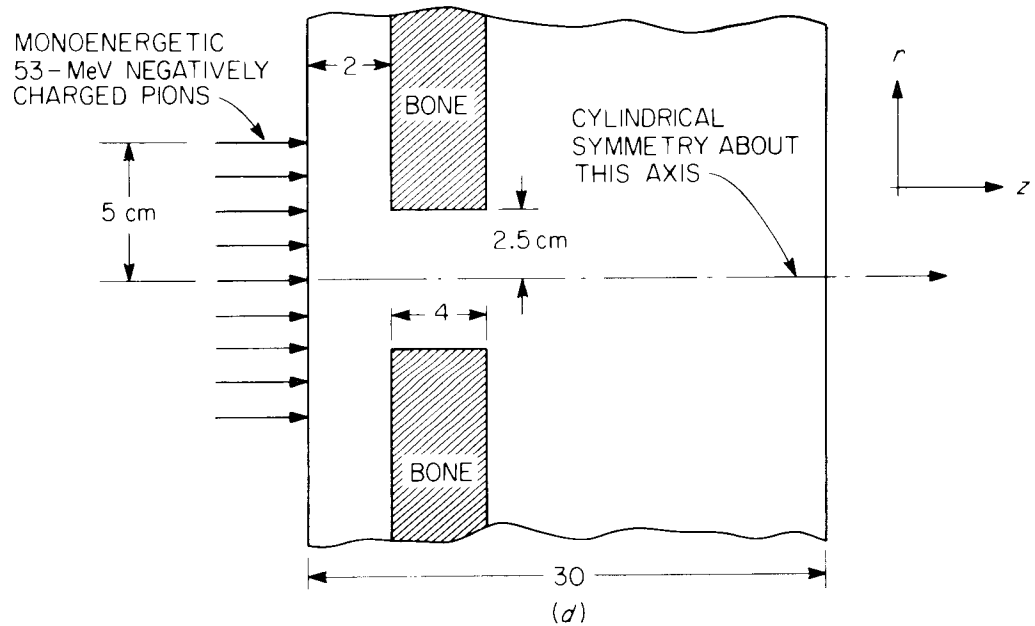


Fig. 1. Schematic diagram of the geometries used in the calculations.

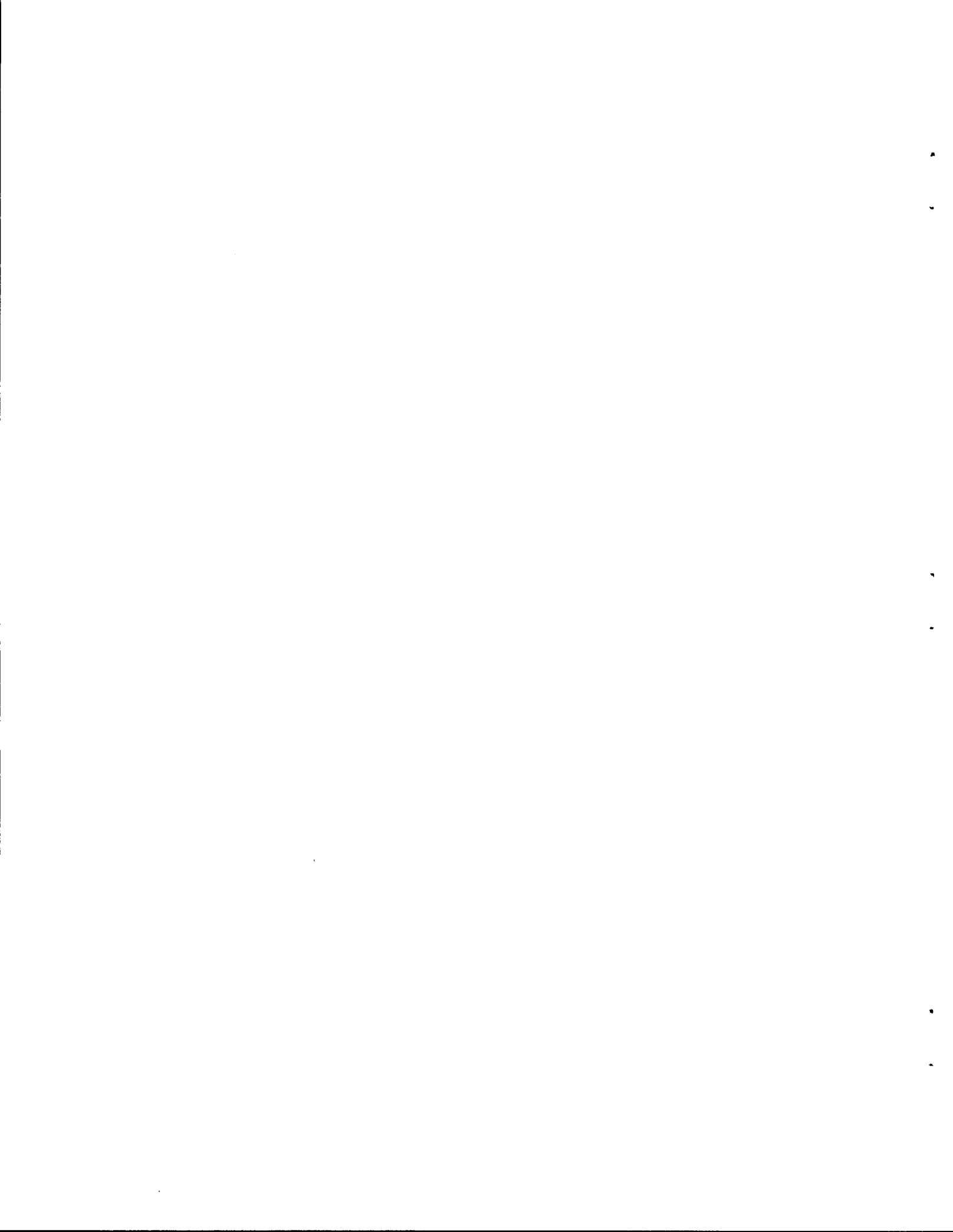
Table 1. Composition of Tissue and Bone

Element	Density of Nuclei (nuclei cm ⁻³)	
	Tissue ^a ($\rho = 1.0 \text{ g cm}^{-3}$)	Bone ^b ($\rho = 1.85 \text{ g cm}^{-3}$)
H	6.265×10^{22}	7.074×10^{22}
C	9.398×10^{21}	2.851×10^{22}
N	1.342×10^{21}	2.148×10^{21}
O	2.551×10^{22}	2.855×10^{22}
Mg		9.156×10^{19}
P		2.518×10^{21}
S		6.953×10^{19}
Ca		4.086×10^{21}

a. See Alsmiller, Armstrong and Coleman 1970.

b. See Janni 1966.

In all cases, the negatively charged pion beams were taken to be normally incident on the surface of the phantoms. Only monoenergetic (53 MeV) uncontaminated pion beams were considered. The range of 53-MeV pions in tissue is approximately 10 g cm^{-2} . In actual practice, negatively charged pion beams would be contaminated with both electrons and negatively charged muons and have an energy spread determined by the quality and limitations of the beam-transport system. For configurations (a), (b), and (c) in fig. 1, a zero-width pion beam was assumed, while for configuration (d), the pions were assumed to be uniformly distributed over a circular area defined by a radius of 5 cm and to be zero outside of this area.



3. RESULTS AND DISCUSSION

3.1 Semi-infinite "Thin" Bone Slabs

The results presented in this section are for the phantoms shown in the upper portion of fig. 1.* The absorbed dose is shown in fig. 2 as a

*Configuration (a) has previously been discussed in detail by Armstrong, Alsmiller, and Chandler (1973).

function of depth in several radial intervals about the beam axis for the three geometries considered. In fig. 2 the absorbed dose is plotted in units of $[\text{erg cm}^{-3} (\text{incident pion})^{-1}]$ to eliminate any ambiguities due to density and the depth is given in g cm^{-2} . The solid histograms show the results obtained for the geometry in fig. 1 (a), the dashed histograms give the results for the geometry in fig. 1 (b), and the circles, the midpoints of the histograms, are the results for the geometry in fig. 1 (c). For the bone in the central region of the phantom [fig. 1 (c)], the absorbed dose as a function of depth is shown for only the radial intervals of 0 to 0.5 cm and 0.5 to 1.0 cm since at the larger radii meaningful statistical accuracy was not obtained. In fig. 2 and throughout the paper, the error bars, where shown, are statistical and represent one standard deviation.

In fig. 2 the absorbed dose in the radial interval of 0 to 0.5 cm has a local minimum in the depth interval of 8 to 9 g cm^{-2} . This minimum is due to the removal of pions from this radial interval by multiple Coulomb scattering. At larger radii (> 0.5 cm), there is a rapid increase in the absorbed dose with increasing depth to a depth of approximately 10 g cm^{-2} , which is the mean range of the incident pions. In all of the results shown

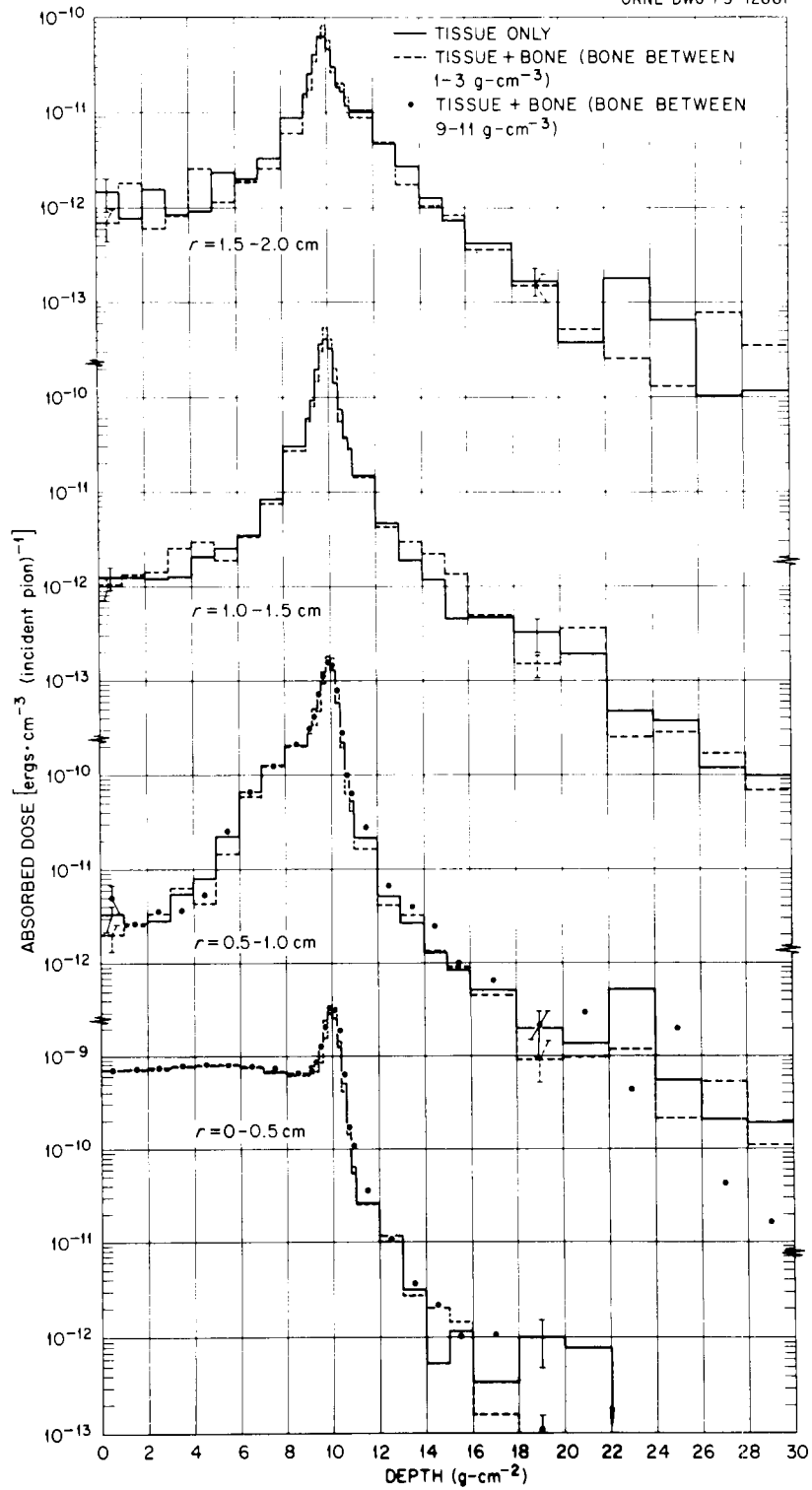


Fig. 2. Absorbed dose vs depth in various radial intervals for incident negatively charged pions.

in fig. 2, the differences in the absorbed dose are within the statistical precision of the calculations, and thus for the configurations considered the presence of bone has no appreciable effect on the absorbed dose when the absorbed dose is considered as a function of depth in g cm^{-2} . The results shown in fig. 2 with bone present and absent would appear very different if depth were measured in cm in the two different configurations. Results very similar to those shown in fig. 2 can be obtained as a function of depth in cm if the decision is made to measure this depth in cm in only configuration (b). To understand this, note that if $\rho(r,z)$ is the density in configuration (b), then the equation (see sec. 2)

$$z' = \int_0^z \rho(r,z'') dz''$$

is a point transformation from depth in cm to depth in g cm^{-2} in this configuration, and this transformation may be applied to all the data in fig. 2 to obtain the absorbed dose as a function of depth in cm measured in configuration (b).

In fig. 3 the cell-survival probabilities for aerobic T-1 kidney cells in the geometries shown in fig. 1 as (a) and (b) are plotted as a function of depth in g cm^{-2} for several radial intervals. The solid and dashed histograms have the same meanings as those in fig. 2. The calculational methods, discussed by Armstrong and Chandler (1973), for estimating the cell-survival probability do not presently include mechanisms for calculating cell survival in bone. Therefore, no cell-survival results are given in the shaded area in fig. 3 for the geometry with bone included, and no cell-survival probabilities have been calculated for the geometry given in fig. 1 (c). For both geometries considered in fig. 3, the cell-survival

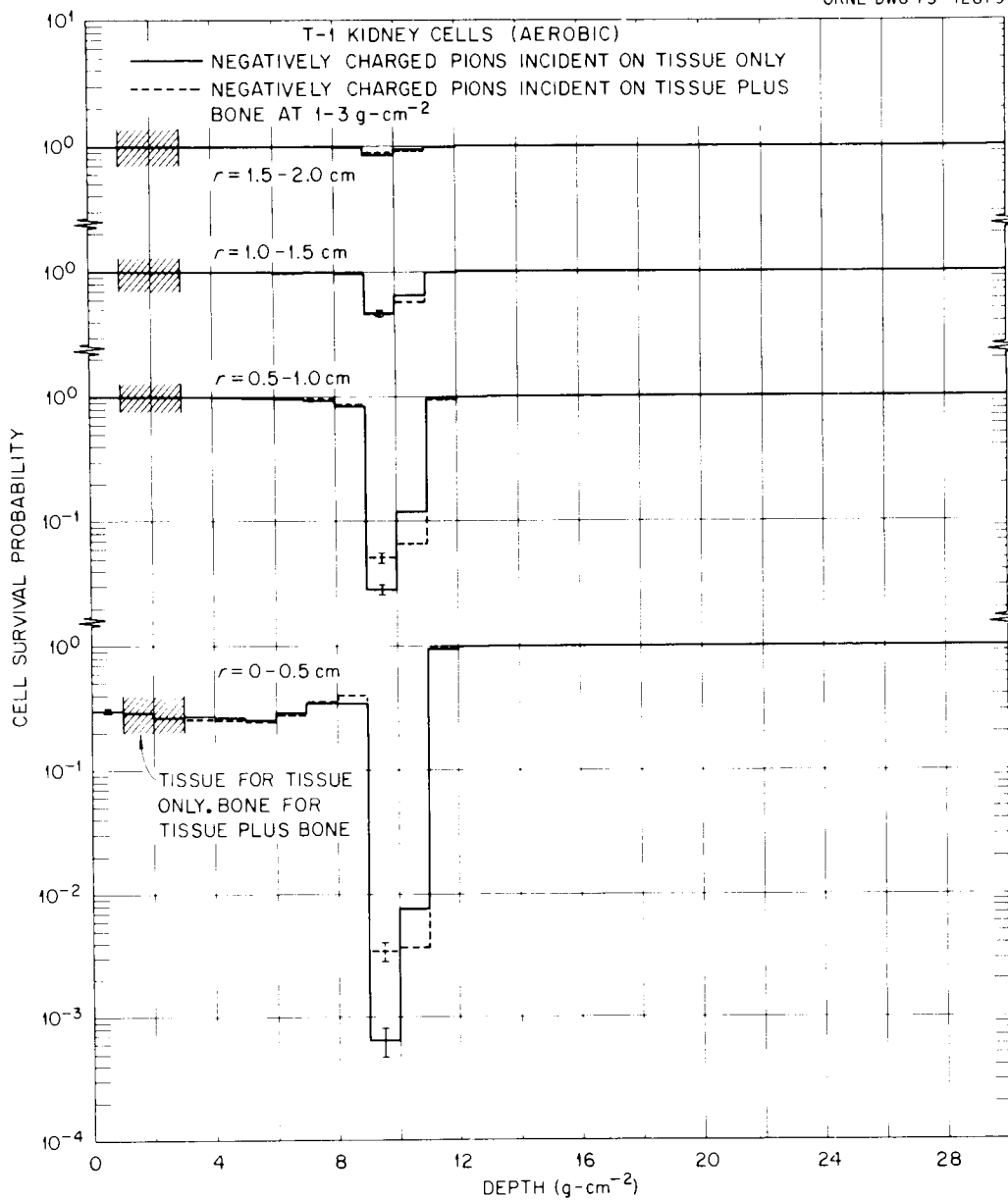


Fig. 3. Cell-survival probability for aerobic T-1 kidney cells vs depth for several radial intervals. The cell-survival probability is taken to be 0.30 in the depth interval of 0 to 1.0 cm and in the radial interval of 0 to 0.5 cm. The cross-hatched areas indicate the bone thickness for the results with bone included.

probability in the depth interval of 0 to 1.0 g cm⁻² and in the radial interval of 0 to 0.5 cm has been taken to be 0.30. The maximum in the cell-survival probability in the radial interval of 0 to 0.5 cm and the depth interval of 8 to 9 g cm⁻² is correlated with the local minimum in the absorbed dose in this region shown in fig. 2 and is due to the fact that particles are being lost from the radial interval of 0 to 0.5 by multiple Coulomb scattering.

The cell-survival probability for anoxic T-1 kidney cells is shown in fig. 4 as a function of depth in g cm⁻² in several radial intervals for geometries (a) and (b) in fig. 1. The absorbed-dose values used in the calculations of these data are the same as those used to obtain the data shown in fig. 3.

In both figs. 3 and 4, the calculations with bone present and absent are in agreement except at small radii in the depth interval of 9 to 11 g cm⁻² where the cell-survival probability is very small. Thus to some extent, the effects of bone on cell survival for the configurations considered can be approximated by considering the cell-survival probability as a function of depth in g cm⁻², but the approximation may not be adequate in those regions where the cell-survival probability is small (≤ 0.1 for the configurations considered in figs. 3 and 4).

In table 2 are listed the OER and RBE values at the 10% survival level in the indicated spatial regions (depth measured in g cm⁻²) for geometries (a) and (b) of fig. 1. For the depth and radial intervals considered, there are few, if any, differences between the values in table 2 with bone present and absent which are not within the statistical accuracy of the calculations. In particular, the difference between the anoxic RBE's with bone present and

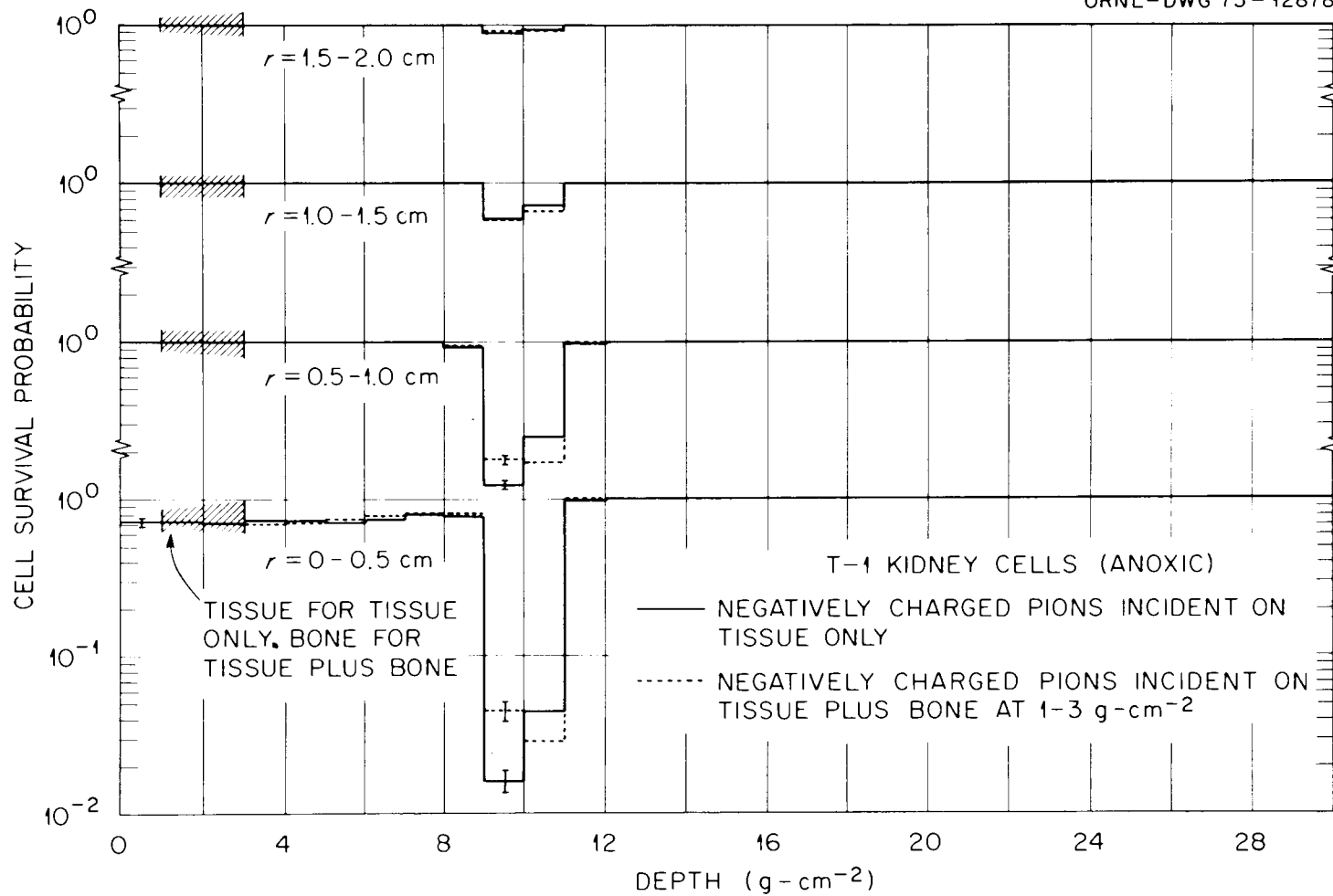


Fig. 4. Cell-survival probability for anoxic T-1 kidney cells vs depth for several radial intervals. The absorbed-dose values are the same as those used for fig. 3.

Table 2. OER and RBE Values at 10% Survival Level for T-1 Kidney Cells Averaged Over the Indicated Spatial Intervals

Depth Interval (g cm ⁻²)	OER	RBE T-1 Kidney Cells	
		Aerobic	Anoxic
<u>Radial Interval = 0 - 0.5 cm</u>			
4 - 9	2.6 ^a	1.0 ^a	1.1
	2.6	1.0	1.1
9 - 11	1.6	2.1	3.8
	1.6	2.2	3.8
11 - 30	2.0	1.4	1.8
	1.8	1.6	2.5
<u>Radial Interval = 0.5 - 1.0 cm</u>			
4 - 9	2.4	1.1	1.2
	2.4	1.1	1.2
9 - 11	1.6	2.2	3.9
	1.5	2.2	3.9
11 - 30	1.8	1.6	2.4
	1.8	1.6	2.4
<u>Radial Interval = 1.0 - 1.5 cm</u>			
4 - 9	2.0	1.4	1.8
	2.0	1.4	1.9
9 - 11	1.5	2.2	3.9
	1.6	2.2	3.8
11 - 30	1.8	1.7	2.5
	1.8	1.6	2.4
<u>Radial Interval = 1.5 - 2.0 cm</u>			
4 - 9	1.6	2.0	3.2
	1.7	1.8	2.9
9 - 11	1.6	2.0	3.4
	1.6	2.0	3.4
11 - 30	1.7	1.7	2.8
	1.8	1.7	2.6

a. The upper values are those obtained with configuration (b) of fig. 1 which includes bone, and the lower values are those obtained for configuration (a) of fig. 1 which includes only tissue.

and absent in the depth interval of 11 to 30 g cm^{-2} and in the radial interval of 0 to 0.5 cm is thought to be due primarily to poor statistical accuracy. The differences in cell-survival probabilities with bone present and absent at small radii in the depth interval of 9 to 11 g cm^{-2} in figs. 3 and 4 are not very apparent in the results given in table 2 because the values in the table have been obtained by averaging over the depth interval of 9 to 11 g cm^{-2} .

3.2 Bone-Tissue Interfaces

The results reported in this section were obtained for geometry (d) shown in fig. 1.

Shown in fig. 5 is the radially integrated absorbed dose as a function of depth in the phantom. The solid histograms are due to pions incident on the phantom with bone and the dashed histograms correspond to the geometry where the bone in fig. 1 (d) is replaced with tissue. The absorbed dose is plotted in units of $[\text{erg cm}^{-1}(\text{incident pion})^{-1}]$ to eliminate any ambiguities due to density and the depth is given in cm. Pions incident on the geometry with bone included give rise to two peaks: one due to the pions passing through the bone at values of $r > 2.5$ cm and a second due to pions passing through the hole in the bone at values of $r < 2.5$ cm. Since the density of bone is different from that of tissue, the pions that pass through the bone are slowed down more rapidly than those passing only through tissue, and they come to rest and are captured at shallower depths in the phantom.

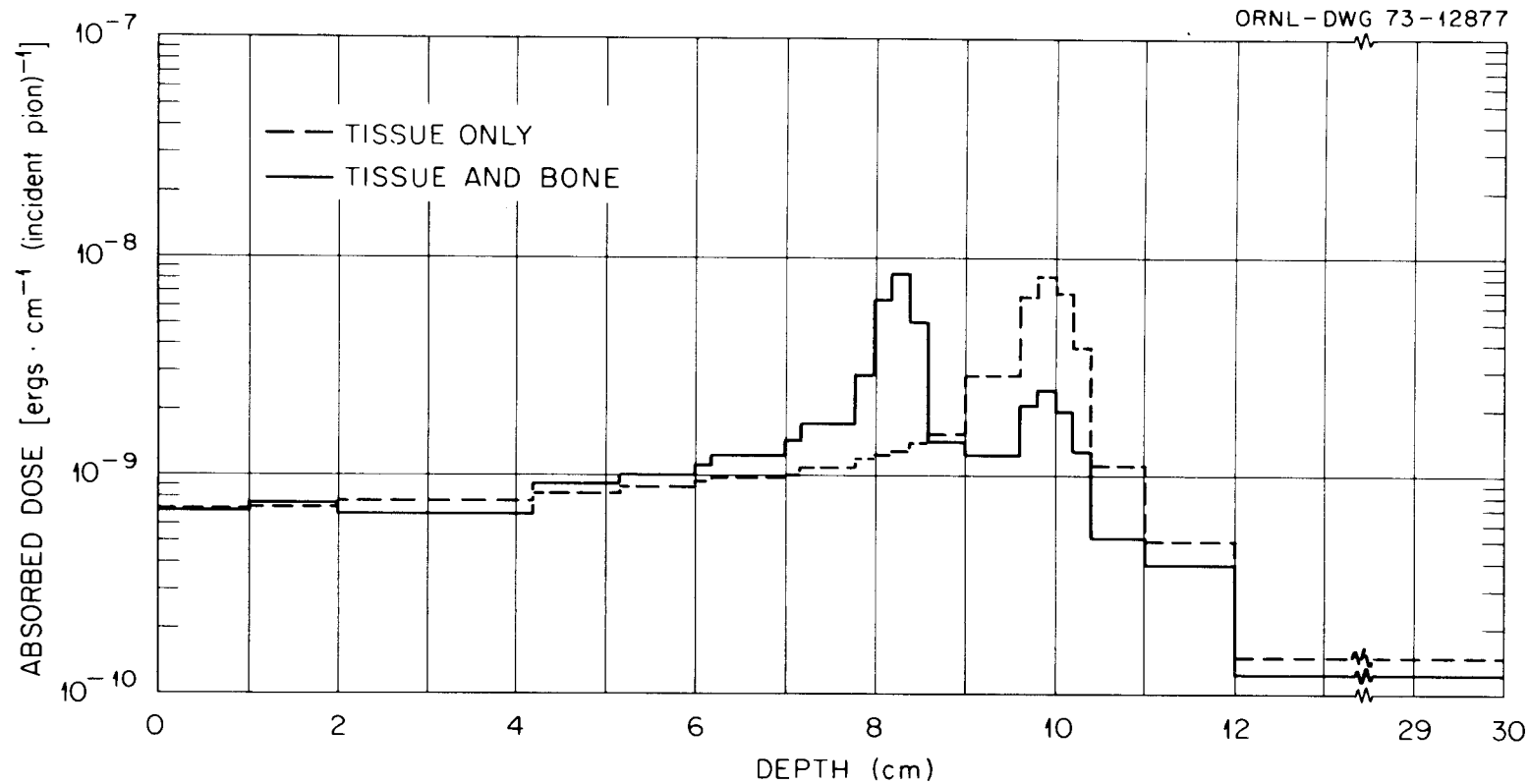


Fig. 5. Radially integrated absorbed dose vs depth for negatively charged pions incident on tissue with bone included and on tissue only. The incident-pion-beam radius was taken to be 5.0 cm.

In fig. 6 the absorbed dose is plotted as a function of radius for several depths in the phantom. The solid histograms give the absorbed dose with bone included and the dashed histograms are the results of "scaling" radial absorbed-dose distributions produced in a homogeneous tissue phantom. The scaling procedure is based on measuring depth in g cm^{-2} , as in the previous section, but is somewhat more complicated here because of the complicated geometry. The procedure used is described in detail below.

The effect on the radial absorbed-dose distributions of the bone-tissue interface at $r = 2.5$ cm and of bone at $r > 2.5$ cm is evident in the data (solid histograms in fig. 6), particularly as the depth increases. At radii < 2.5 cm at all depths considered except the largest, there are contributions to the absorbed dose from particles which have passed through the bone and have been scattered into this region, and at all depths shown there are contributions to the absorbed dose at radii > 2.5 cm from particles which have passed through the hole in the bone and have been scattered to larger radii. It is the presence of these contributions from scattered particles which makes the use of depth measured in g cm^{-2} more complicated in the present case than in the cases treated in sec. 3.1. Those pions which have passed through the bone must have associated with them, irrespective of radius, a depth in g cm^{-2} which includes the bone, and those pions which have passed through the hole in the bone must have associated with them, irrespective of radius, a depth in g cm^{-2} which does not include the bone. There are, of course, some incident pions with radii near 2.5 cm which are scattered from tissue into bone and from bone into tissue, and it is not possible to associate with these particles an unambiguous depth in g cm^{-2} .

The dashed histograms in fig. 6 were obtained by "scaling" absorbed-dose radial distributions obtained by replacing the bone in fig. 1 (d) with tissue. The procedure used was to carry out separate calculations, with the tissue slab, for those incident particles with radii < 2.5 cm and those incident particles with radii > 2.5 cm. The incident pions with radii > 2.5 cm correspond to those which would pass through the bone if it were present. Using these results, the dashed histogram in fig. 6 at a depth X in cm is obtained by adding the radial absorbed-dose distribution at X g cm⁻² from those incident particles with radii < 2.5 cm to the radial absorbed-dose distribution at Y g cm⁻² from those incident particles with radii > 2.5 cm with Y given by

$$Y = X + 2.138 (\rho_B - \rho_T) ,$$

where 2.138 is the bone thickness in cm and ρ_B and ρ_T are the densities of bone and tissue, respectively. It should be noted that the radial distributions at X and at Y have values at all radii because of the effects of pion multiple Coulomb scattering and because of contributions from nuclear-reaction products.

The difference between the solid and dashed histograms in fig. 6 is a function of both depth and radius. At small radii and at all depths, the major contribution to the absorbed dose is from pions which have passed through tissue only, and the solid and dashed histograms are in agreement. At the larger radii where the contributions to the solid histograms from pions which have passed through bone are large, there are substantial differences between the solid and dashed histograms at some depths but particularly in the depth interval of 7.76 to 7.96 cm which corresponds to a depth interval of 9.60 to 9.80 g cm⁻² measured through the bone.

These differences at the larger radii can be understood, at least in part, on the basis of the difference in the mass stopping powers of bone and tissue. This difference in mass stopping power gives rise to a difference in the mean range of those pions which pass through bone and those pions which pass through tissue only, and this causes a substantial difference in the absorbed-dose distribution at some depth near the end of the pion range. This is shown in fig. 7 where the absorbed dose is given as a function of depth in the radial intervals of 0 to 1.0 cm and 3.0 to 4.0 cm. The solid histograms show the results for configuration (d) in fig. 1 and the dashed histograms show the results for the case of tissue. In the radial interval of 0 to 1.0 cm, the absorbed dose in both cases is due primarily to pions which pass through tissue only, and thus the solid and dashed histograms are in substantial agreement. In the radial interval of 3.0 to 4.0 cm, there are substantial differences between the solid and dashed histograms, particularly in the vicinity of the peak absorbed dose, due to the differences in stopping powers of bone and tissue. These differences in the absorbed-dose histograms in the radial interval of 3.0 to 4.0 cm are responsible, to some extent at least, for the differences between the solid and dashed histograms at the larger radii in fig. 6.

Irrespective of the cause, the solid and dashed histograms in fig. 6 do not agree well, and thus for the configuration considered, the "scaling" procedure used is not entirely satisfactory for treatment-planning purposes. On the basis of the discussion above, it might be possible to introduce additional corrections into the scaling procedure to account for differences in stopping powers, but this would require information in addition to thickness in g cm^{-2} and for this reason is not considered here.

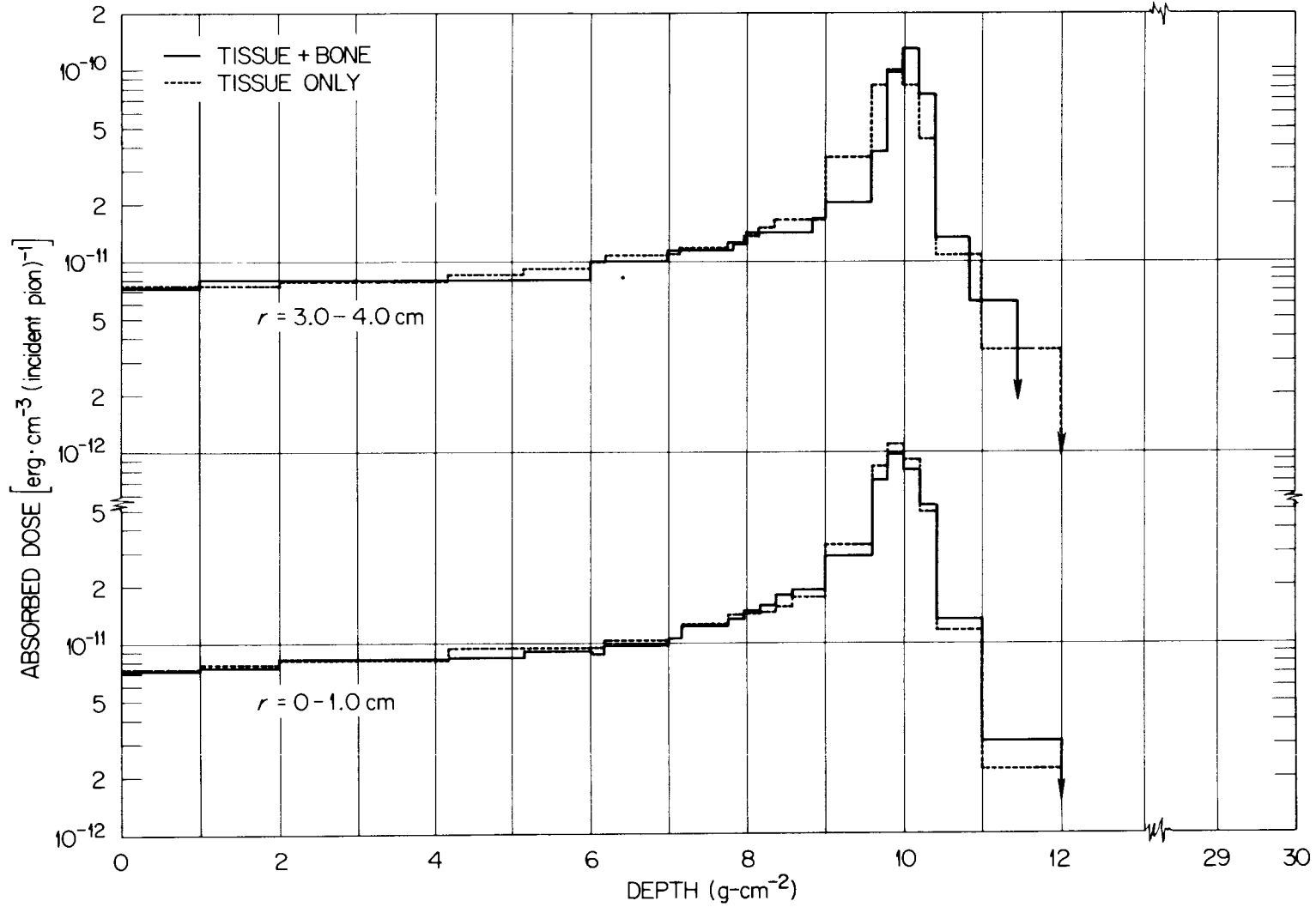


Fig. 7. Absorbed dose vs depth.

When bone is present, the mean range in g cm^{-2} of incident pions and the displacement in depth of the peak in the absorbed dose, such as that shown in the radial interval of 3.0 to 4.0 cm in fig. 6, are dependent on the thickness of bone. In table 3 the variation of the mean range in g cm^{-2} of 53-MeV pions due to the presence of bone is given for several bone thicknesses. In sec. 3.1 where a bone thickness of 2 g cm^{-2} was considered, an effect such as that shown in the upper histogram in fig. 7 should have been present, but it was smaller there and was masked by the width of the histogram intervals. From the results given in sec. 3.1 and in table 3, it can be anticipated that the "scaling" procedure used to produce the results in fig. 6 will become more satisfactory if bone thicknesses of $< 4 \text{ g cm}^{-2}$ are considered.

The cell-survival probability for aerobic T-1 kidney cells is shown in fig. 8 as a function of radius for several depth intervals. The histograms in fig. 8 have the same meanings as those in fig. 6; i.e., the solid histograms were obtained with configuration (d) in fig. 1 and the dashed histograms were obtained with a tissue phantom and the scaling procedure described previously. The results in fig. 8 with bone included (solid histograms) have been normalized to 0.1 in the depth interval of 9.8 to 10.0 cm and in the radial interval of 0 to 1.0 cm. The dashed histograms were normalized to the same number of incident pions as was used in obtaining the solid histograms. The effect of the tissue-bone interface at 2.5 cm is very evident in the solid histograms in fig. 8. The differences between the solid and dashed histograms in fig. 8 are similar as a function of depth and radius to those shown in fig. 7, but the magnitude of the differences in fig. 8 is often larger than the magnitude of the differences in fig. 6.

Table 3. The Variation in the Mean Range of Negatively Charged Pions in Tissue Due to the Presence of Bone^a

Bone Thickness (g cm ⁻²)	Mean Range ^b (g cm ⁻²)
0	10.00
2	10.08
4	10.16

- a. The bone was inserted in the tissue at a depth of 1.0 g cm⁻².
- b. The incident pion energy was selected to have a mean range in tissue of 10 g cm⁻².

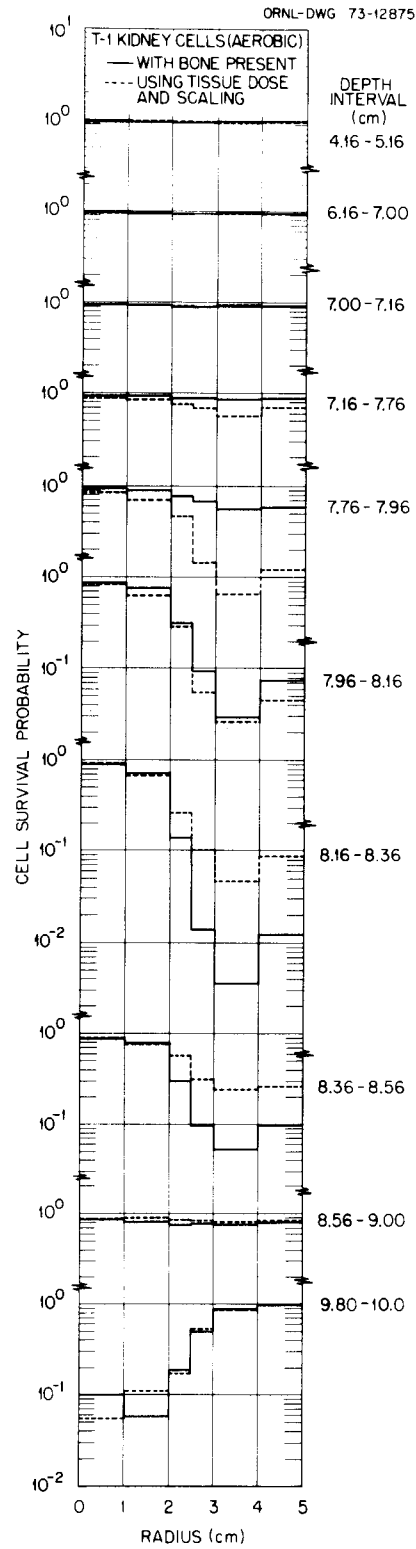


Fig. 8. Cell-survival probability for aerobic T-1 kidney cells as a function of radius for several depth intervals.

The cell-survival probability for anoxic T-1 kidney cells is shown in fig. 9 as a function of radius for several depths. The solid and dashed histograms in fig. 9 have the same meanings as those in fig. 8, and the normalization used (number of incident pions) is the same in fig. 9 as that in fig. 8. Qualitatively, the results in fig. 9 are similar to those in fig. 8.

In tables 4 through 6 the OER and RBE values, respectively, are given as a function of depth and radius. In these tables, the upper values for each depth and radial interval are the results for configuration (d) in fig. 1 and the lower values are those obtained with the tissue phantom and the scaling procedure described earlier. On the basis of the results shown in figs. 7 and 8, there are, as one would expect, some significant differences between the values obtained with bone present and those given by the scaling procedure. The conclusions to be drawn from figs. 7 and 8 and from tables 4 through 6 are essentially the same as those drawn following the discussion of fig. 6. For the configuration considered here, the scaling procedure is not very satisfactory. In considering the results, however, it should be noted that the use of monoenergetic incident pions and the use of a large bone thickness provide a very stringent test of the procedure, and for this reason the results obtained cannot be considered to be representative of those that might be obtained under less stringent conditions.

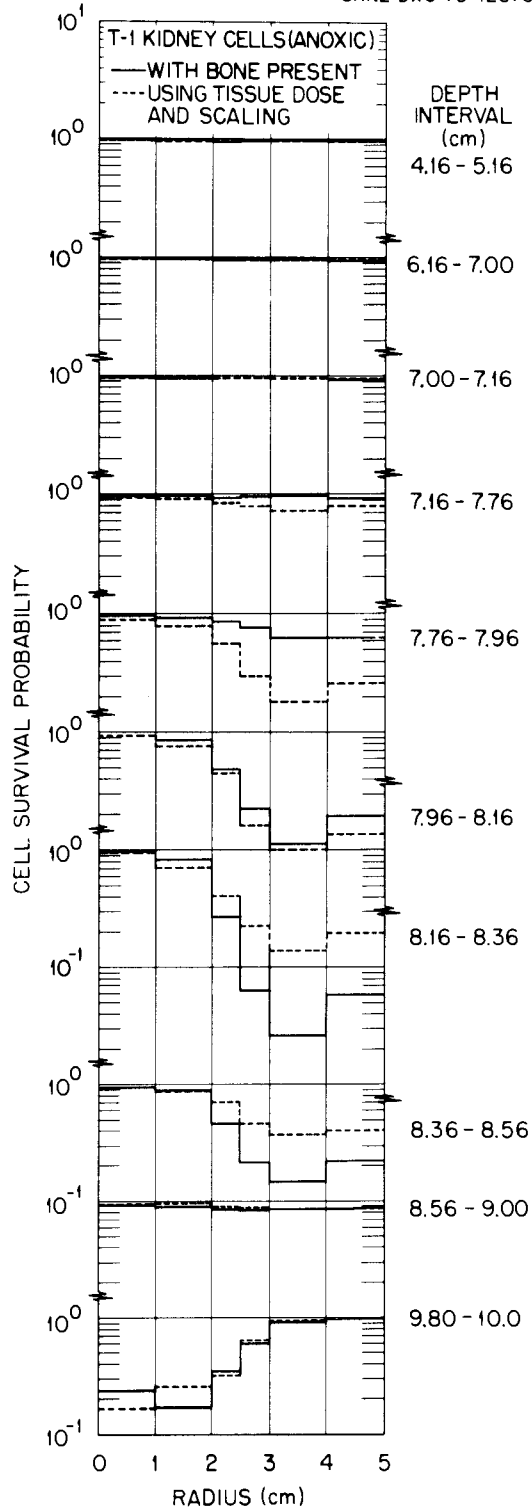


Fig. 9. Cell-survival probability for anoxic T-1 kidney cells as a function of radius for several depth intervals.

Table 4. OER Values at 10% Survival Level for T-1 Kidney Cells Averaged Over the Indicated Spatial Intervals

Depth Interval (cm)	OER					
	Radial Interval (cm)					
	0-1.0	1.0-2.0	2.0-2.5	2.5-3.0	3.0-4.0	4.0-5.0
4.16 - 5.16	2.3 ^a	2.3	2.2	2.3	2.4	2.4
	2.4	2.3	2.3	2.4	2.3	2.3
6.16 - 7.00	2.4	2.3	2.2	2.3	2.4	2.4
	2.3	2.3	2.3	2.3	2.3	2.3
7.00 - 7.16	2.2	2.3	2.2	2.3	2.3	2.3
	2.3	2.3	2.2	2.3	2.4	2.3
7.16 - 7.76	2.3	2.3	2.2	2.3	2.3	2.3
	2.2	2.1	1.9	1.9	1.8	1.9
7.76 - 7.96	2.4	2.3	2.1	1.9	1.9	1.8
	2.0	1.8	1.6	1.6	1.6	1.6
7.96 - 8.16	2.1	1.9	1.6	1.6	1.5	1.5
	2.2	1.8	1.6	1.5	1.5	1.5
8.16 - 8.36	2.3	1.9	1.5	1.5	1.5	1.5
	2.2	1.8	1.5	1.5	1.5	1.5
8.36 - 8.56	2.3	2.0	1.6	1.5	1.5	1.5
	2.2	1.9	1.7	1.5	1.5	1.5
8.56 - 9.00	2.2	2.1	1.9	1.8	1.7	1.6
	2.3	2.3	2.0	1.8	1.6	1.6
9.80 - 10.00	1.6	1.5	1.6	1.5	1.7	1.7
	1.5	1.6	1.5	1.6	1.6	1.7

a. The upper values are those obtained with configuration (d) of fig. 1 which includes bone and the lower values are those obtained using a tissue phantom and the scaling procedure described in the text.

Table 5. RBE Values for Aerobic T-1 Kidney Cells at 10% Survival Level Averaged Over the Indicated Spatial Intervals

Depth Interval (cm)	RBE					
	Radial Interval (cm)					
	0-1.0	1.0-2.0	2.0-2.5	2.5-3.0	3.0-4.0	4.0-5.0
4.16 - 5.16	1.1 ^a	1.2	1.2	1.2	1.1	1.1
	1.1	1.2	1.2	1.1	1.2	1.2
6.16 - 7.00	1.1	1.2	1.2	1.2	1.1	1.1
	1.2	1.3	1.2	1.2	1.2	1.2
7.00 - 7.16	1.2	1.2	1.3	1.2	1.2	1.2
	1.2	1.1	1.2	1.2	1.1	1.2
7.16 - 7.76	1.2	1.1	1.2	1.2	1.2	1.2
	1.3	1.3	1.4	1.5	1.6	1.5
7.76 - 7.96	1.1	1.2	1.3	1.5	1.5	1.6
	1.4	1.6	2.0	2.2	2.2	2.3
7.96 - 8.16	1.3	1.5	2.0	2.3	2.3	2.3
	1.2	1.7	2.0	2.4	2.5	2.5
8.16 - 8.36	1.2	1.5	2.4	2.6	2.6	2.6
	1.2	1.6	2.3	2.4	2.5	2.6
8.36 - 8.56	1.2	1.3	2.2	2.5	2.6	2.6
	1.2	1.5	1.8	2.3	2.5	2.6
8.56 - 9.00	1.3	1.3	1.5	1.7	1.9	2.0
	1.2	1.2	1.4	1.7	1.9	2.1
9.80 - 10.00	2.2	2.3	2.2	2.2	1.9	1.8
	2.2	2.2	2.3	2.2	2.0	1.7

a. The upper values are those obtained with configuration (d) of fig. 1 which includes bone and the lower values are those obtained using a tissue phantom and the scaling procedure described in the text.

Table 6. RBE Values for Anoxic T-1 Kidney Cells at 10% Survival Level Averaged Over the Indicated Spatial Intervals

Depth Interval (cm)	RBE					
	Radial Interval (cm)					
	0-1.0	1.0-2.0	2.0-2.5	2.5-3.0	3.0-4.0	4.0-5.0
4.16 - 5.16	1.3 ^a	1.4	1.5	1.4	1.3	1.3
	1.2	1.4	1.4	1.3	1.4	1.4
6.16 - 7.00	1.2	1.4	1.5	1.4	1.3	1.3
	1.3	1.3	1.4	1.4	1.3	1.4
7.00 - 7.16	1.4	1.4	1.6	1.4	1.4	1.4
	1.3	1.3	1.5	1.4	1.3	1.4
7.16 - 7.76	1.4	1.3	1.5	1.4	1.4	1.3
	1.6	1.6	2.0	2.2	2.3	2.0
7.76 - 7.96	1.2	1.4	1.8	2.1	2.0	2.3
	2.0	2.5	3.3	3.8	4.0	3.9
7.96 - 8.16	1.7	2.0	3.3	3.9	4.1	4.1
	1.5	2.6	3.6	4.2	4.5	4.7
8.16 - 8.36	1.4	2.0	4.3	4.8	4.9	4.8
	1.4	2.4	4.0	4.3	4.6	4.7
8.36 - 8.56	1.5	1.8	3.7	4.6	4.8	4.8
	1.3	2.0	3.0	4.1	4.5	4.7
8.56 - 9.00	1.6	1.6	2.0	2.6	3.0	3.3
	1.4	1.4	1.9	2.5	3.2	3.6
9.80 - 10.00	3.8	4.0	3.8	3.9	3.1	2.8
	3.9	3.8	4.1	3.7	3.5	2.7

a. The upper values are those obtained with configuration (d) of fig. 1 which includes bone and the lower values are those obtained using a tissue phantom and the scaling procedure described in the text.

REFERENCES

- ALSMILLER, R. G., Jr., ARMSTRONG, T. W., and COLEMAN, W. A., 1970, Nucl. Sci. Eng. 42, 367.
- ALSMILLER, R. G., Jr. and BARISH, J., 1974, ORNL-TM-4442, Oak Ridge National Laboratory.
- ARMSTRONG, T. W., ALSMILLER, R. G., Jr., CHANDLER, K. C., and BISHOP, B. L., 1972, Nucl. Sci. Eng. 49, 82.
- ARMSTRONG, T. W., ALSMILLER, R. G., Jr., and CHANDLER, K. C., 1973, Phys. Med. Biol. 18, 830.
- ARMSTRONG, T. W., and BISHOP, B. L., 1971, Radiat. Res. 47, 581.
- ARMSTRONG, T. W., and CHANDLER, K. C., 1972, Radiat. Res. 52, 247.
- ARMSTRONG, T. W., and CHANDLER, K. C., 1973, ORNL-TM-4294, Oak Ridge National Laboratory.
- CHANDLER, K. C., and ARMSTRONG, T. W., 1972, ORNL-4744, Oak Ridge National Laboratory.
- FOWLER, P. H., and PERKINS, D. H., 1961, Nature 189, 524.
- JANNI, J. F., 1966, AFWL-TR-65-150, Air Force Weapons Laboratory.
- KATZ, R., ACKERSON, B., HOMAYOONFAR, M., and SHARMA, S. C., 1971, Radiat. Res. 47, 402.
- KATZ, R., SHARMA, S. C., and HOMAYOONFAR, M., 1972, Chapter 6 of Topics in Radiation Dosimetry, Suppl. 1 to Radiation Dosimetry, Ed. Frank A. Attix, Academic Press, New York.
- RAJU, M. R., and RICHMAN, C., 1970, in Proc. XIIth Intl. Congress of Radiology, Tokyo, 1969, GANN Monograph No. 9, 105.
- ROSEN, Louis, 1968, Nucl. Appl. 5, 379.



Internal Distribution

- | | | | |
|--------|----------------------|--------|--|
| 1-3. | L. S. Abbott | 42. | RSIC |
| 4. | F. S. Alsmiller | 43-57. | R. T. Santoro |
| 5-19. | R. G. Alsmiller, Jr. | 58. | S. Siegel |
| 20. | T. W. Armstrong | 59. | J. B. Storer |
| 21. | J. A. Auxier | 60. | D. Sundberg |
| 22. | J. Barish | 61. | J. R. Totter |
| 23. | H. W. Bertini | 62. | J. E. Turner |
| 24. | A. A. Brooks | 63. | G. E. Whitesides |
| 25. | H. P. Carter | 64. | H. A. Wright |
| 26-30. | K. C. Chandler | 65. | A. Zucker |
| 31. | G. T. Chapman | 66. | H. Feshbach (consultant) |
| 32. | C. E. Clifford | 67. | P. F. Fox (consultant) |
| 33. | T. A. Gabriel | 68. | A. F. Henry (consultant) |
| 34. | R. N. Hamm | 69. | W. W. Havens, Jr. (consultant) |
| 35. | O. W. Hermann | 70-71. | Central Research Library |
| 36. | T. D. Jones | 72. | ORNL Y-12 Technical Library,
Document Reference Section |
| 37. | N. M. Larson | 73-74. | Laboratory Records Department |
| 38. | J. L. Lucius | 75. | Laboratory Records ORNL RC |
| 39. | F. C. Maienschein | 76. | ORNL Patent Office |
| 40. | R. W. Peelle | | |
| 41. | R. W. Roussin | | |

External Distribution

77. H. Goldstein, Columbia University, New York, New York, 10027.
78. W. W. Hannum, Division of Reactor Research and Development,
U. S. Atomic Energy Commission, Washington, D. C., 20545.
79. P. B. Hemmig, Division of Reactor Research and Development,
U. S. Atomic Energy Commission, Washington, D. C., 20545.
80. J. L. Liverman, Division of Biomedical and Environmental Research,
U. S. Atomic Energy Commission, Washington, D. C., 20545.
81. Kermit Laughon, AEC Site Representative.
82. Dr. R. Vasudevan, Institute of Mathematical Sciences, Adyar,
Madras, India.
- 83-171. Given National Science Foundation Distribution (see pp. 35-37)
- 172-173. Technical Information Center (TIC).
174. Research and Technical Support Division (ORO).

NATIONAL SCIENCE FOUNDATION DISTRIBUTION

1. Dr. Peter R. Almond, MD Anderson Hospital and Tumor Institute, The University of Texas, 6723 Bertner Boulevard, Houston, Texas 77025
2. Dr. Frank H. Attix, U. S. Naval Research Laboratory, Washington, D. C. 20390
3. Dr. Miguel Awschalom, Head, Radiation Physics Section, National Accelerator Laboratory, P. O. Box 500, Batavia, Illinois 50410
4. Dr. Johan Baarli, Head, Health Physics Division, CERN, Geneva 23, SWITZERLAND
5. Dr. M. A. Bagshaw, Department of Radiology, Stanford School of Medicine, Stanford, California 94305
6. Dr. G. W. Barendsen, Radiobiological Institute of the Organization for Health Research TNO, 151 Lange Kleiweg, Rijswijk (Z-H), THE NETHERLANDS
7. Dr. Nathaniel F. Barr, Assistant Director for Measurement and Evaluation, Division of Biomedical and Environmental Research, U. S. Atomic Energy Commission, Washington, D. C. 20545
8. Dr. H. F. Batho, The British Columbia Cancer Institute, 2656 Heather Street, Vancouver 9, BRITISH COLUMBIA
9. Dr. Gerald W. Bennett, Brookhaven National Laboratory, Upton, New York 11973
10. Dr. Martin J. Berger, Radiation Theory Section, National Bureau of Standards, Washington, D. C.
11. Dr. Hans Bichsel, Medical Radiation Physics, 3711 15th Avenue, N.E., University of Washington, Seattle, Washington 28195
12. Mr. H. Blattmann, Strahlenbiologisches Institute, University of Zurich, Zurich, SWITZERLAND
13. Dr. H. R. Blieden, National Science Foundation, 1800 G Street, N.W., Washington, D. C. 20550
14. Dr. Max L. M. Boone, Director of Radiation Oncology, Arizona Medical Center, Department of Radiology, University of Arizona, Tucson, Arizona 85724
15. Dr. Douglas Boyd, W. W. Hansen Laboratory of Physics, Stanford University, Stanford, California 94305
16. Dr. J. J. Broerse, Radiobiological Institute of the Organization for Health Research TNO, 151 Lange Kleiweg, Rijswijk (Z-H), THE NETHERLANDS
17. Dr. L. Cabeza, Strahlenbiologisches Institut, University of Zurich, Zurich, SWITZERLAND
18. Dr. Randall S. Caswell, Neutron Physics Section, National Bureau of Standards, Washington, D. C. 20234
19. Dr. S. B. Curtis, Lawrence Berkeley Laboratory, Berkeley, California 94720
- 20-39. Mr. Gilbert B. Devey, Program Manager, National Science Foundation, 1800 G Street, N.W., Washington, D. C. 20550
40. Dr. J. F. Dicello, Group MP-3, Los Alamos Scientific Laboratory, Los Alamos, New Mexico 87544
41. Mr. Jean Dutrannois, Health Physics Division, CERN, Geneva 23, SWITZERLAND
42. Dr. Peter Fessenden, Department of Radiology, Stanford University Medical Center, Stanford, California 94305

43. Dr. H. Fritz-Niggli, Strahlenbiologisches Institut, University of Zurich, Zurich, SWITZERLAND
44. Dr. Michael Goiten, Department of Radiation Medicine, Massachusetts General Hospital, Cambridge, Massachusetts 02114
45. Dr. P. Haefeli, SIN, CH-5234, Villigen, SWITZERLAND
46. Dr. J. A. Helland, Group MP-3, Los Alamos Scientific Laboratory, P. O. Box 1663, Los Alamos, New Mexico 87544
47. Dr. G. H. Hinling, Nuclear Structure and Reactions, Nuclear Sciences Division, Naval Research Laboratory, Washington, D. C. 20375
48. Dr. P. D. Holt, U.K. Atomic Energy Authority, Building 364, Harwell, Didcot, Birkshire, ENGLAND
49. Dr. Richard Hutson, Los Alamos Scientific Laboratory, P. O. Box 1663, Los Alamos, New Mexico 87644
50. Dr. Henry S. Kaplan, Department of Radiology, Stanford School of Medicine, Stanford, California 94305
51. Dr. C. J. Karzmark, Department of Radiology, Stanford University Medical Center, Stanford, California 94305
52. Professor Robert Katz, Behlen Laboratory of Physics, University of Nebraska, Lincoln, Nebraska 68508
53. Dr. Nick King, Crocker Nuclear Laboratory, University of California, Davis, Davis, California 95616
54. Dr. Morton M. Kligerman, Director, Cancer Research and Treatment Center, School of Medicine, University of New Mexico, Albuquerque, New Mexico 87115
55. Dr. E. A. Knapp, M.P. Division, Los Alamos Scientific Laboratory, Los Alamos, New Mexico 87544
56. Dr. H. B. Knowles, Physics Department, Washington State University, Pullman, Washington 99163
57. Mr. A. M. Koehler, Synchrocyclotron Laboratory, Harvard University, 44 Oxford Street, Cambridge, Massachusetts 02138
58. Dr. Lawrence H. Lanzl, Argonne Cancer Research Hospital, University of Chicago, Chicago, Illinois 60637
59. Dr. C. C. Lushbaugh, Oak Ridge Associated Universities, P. O. Box 117, Oak Ridge, Tennessee 37038
60. Dr. J. T. Lyman, Lawrence Berkeley Laboratory, Berkeley, California 94720
61. Dr. Richard Madey, Department of Physics, Kent State University, Kent, Ohio 44242
62. Dr. Francis J. Mahoney, Program Director for Radiation, Biology, and Physics, National Cancer Institute, Room 10-A10, Westwood Building, 5333 Westbard Avenue, Bethesda, Maryland 20014
63. Dr. J. E. McLaughlin, Director, Radiation Physics Division, Health and Safety Laboratory, U. S. Atomic Energy Commission, 376 Hudson Street, New York, New York 10014
64. Mr. Keran O'Brien, Radiation Physics Division, Health and Safety Laboratory, U. S. Atomic Energy Commission, 376 Hudson Street, New York, New York 10014
65. Mr. Mudundi R. Raju, Los Alamos Scientific Laboratory, P. O. Box 1663, Los Alamos, New Mexico 87544
66. Dr. J. J. Reidy, Physics Department, University of Mississippi, University, Mississippi 38677

67. Dr. Chaim Richman, Los Alamos Scientific Laboratory, P. O. Box 1663, Los Alamos, New Mexico 87544
68. Dr. Louis Rosen, Los Alamos Scientific Laboratory, P. O. Box 1663, Los Alamos, New Mexico 87544
69. Dr. M. E. Schillaci, Los Alamos Scientific Laboratory, P. O. Box 1663, Los Alamos, New Mexico 87544
70. Dr. Walter Schimmerling, Lawrence Berkeley Laboratory, Bldg. 29-315C, Berkeley, California 94720
71. Dr. Roger Schneider, Bureau of Radiological Health - DEP, 5600 Fishers Lane, Rockville, Maryland 20892
72. Dr. H. Alan Schwettman, W. W. Hansen Laboratories of Physics, Stanford University, Stanford, California 94305
73. Dr. S. C. Sharma, Bethlen Laboratory of Physics, The University of Nebraska, Lincoln, Nebraska 68508
74. Dr. Yaakov Shima, SOREQ Nuclear Research Center, Yvena, ISRAEL
75. Dr. Carl R. Shonk, School of Medicine, University of New Mexico, P. O. Box 283, 915 Stanford Street, N.E., Albuquerque, New Mexico 87106
76. Dr. G. R. Stevenson, CERN-II, Geneva 23, SWITZERLAND
77. Dr. Peter Stiller, IKE, D-7 Stuttgart 80, Pfaffenwaldring 31, GERMANY
78. Dr. A. H. Sullivan, Health Physics Division, CERN, Geneva 23, SWITZERLAND
79. Dr. Richard Theus, U. S. Naval Research Laboratory, Washington, D. C. 20390
80. Dr. Ralph H. Thomas, Health Physics Division, Lawrence Berkeley Laboratory, Berkeley, California 94720
81. Dr. Georg Tisljar, Institute fur Medizin, Kernforschungsanlage, Julich, GERMANY
82. Dr. C. A. Tobias, Biology and Medicine Division, Lawrence Berkeley Laboratory, Berkeley, California 94720
83. Dr. Paul Todd, Biophysics Department, Pennsylvania State University, University Park, Pennsylvania 16802
84. Dr. W. Turkinetz, Laboratory for Nuclear Science, Massachusetts Institute of Technology, Cambridge, Massachusetts 02139
85. Dr. R. Vasudewan, Department of Electrical Engineering, University of Southern California, University Park, Los Angeles, California 90007
86. Dr. George L. Voelz, Los Alamos Scientific Laboratory, P. O. Box 1663, Los Alamos, New Mexico 87544
87. Dr. A. L. Wiley, University of Wisconsin, Madison, Wisconsin 53706
88. Dr. R. W. Wood, Chief, Physics and Instrumentation Branch, Division of Biomedical and Environmental Research, U. S. Atomic Energy Commission, Washington, D. C. 20546
89. Dr. Peter Wootton, Medical Radiation Physics, 3711 15th Avenue, N.E., University of Washington, Seattle, Washington 98194